Steerable Burrowing Robot: Design, Modeling and Experiments

Moran Barenboim and Amir Degani, *Member, IEEE*

Abstract—This paper investigates a burrowing robot that can maneuver and steer while being submerged in a granular medium. The robot locomotes using an internal vibro-impact mechanism and steers using a rotating bevel-tip head. We formulate and investigate a non-holonomic model for the steering mechanism and a hybrid dynamics model for the thrusting mechanism. We perform a numerical analysis of the dynamics of the robot's thrusting mechanism using a simplified, orientation and depth dependent model for the drag forces acting on the robot. We first show, in simulation, that by carefully tuning various control input parameters, the thrusting mechanism can drive the robot both forward and backward. We present several experiments designed to evaluate and verify the simulative results using a proof-of-concept robot. We show that different input amplitudes indeed affect the direction of motion, as suggested by the simulation. We further demonstrate the ability of the robot to perform a simple S-shaped trajectory. These experiments demonstrate the feasibility of the robot's design and fidelity of the model.

I. INTRODUCTION AND RELATED WORK

Locomotion of robots on land, water, and air has been possible for years. However, locomotion underground is a challenging task for robots and has yet to be fully addressed. Underground robots can be useful in several applications, such as laying underground cables, detonating mines, sensing for precision agriculture, or even gas exploration. Several studies were conducted in the field, yet little was reported on the ability of robots to steer underground. The current paper investigates the design and modeling of a simple, self-propelled, steerable robot in granular medium. Several recent studies have focused on locomotion underground, such as drilling robots [1]–[3], biomimetic robots [4], [5] and hammering robots [6]–[8]. Typical drilling robots use a screw-like mechanism to create linear motion in the axial direction. The literature suggests that the latest drilling mechanisms can drill up to twice their own body length but then stop due to actuator limitations [1]. Biology inspired studies allow locomotion that is potentially more energy efficient. Still, such biomimetic robots haven't yet penetrated deeply into the soil [4], [5]. Hammering robots, using impact mechanisms to dig themselves underground, were shown to be able to penetrate substantially deeper than other mechanisms and have the ability to submerge several times their own body length [9].

The basic concept of burrowing robot presented in Becker et al., [1], as well as in other works [2]–[9], are limited to straight trajectories without the ability to steer. A common solution for steering used in the piping industry relies on a mechanism which deforms the main axial shaft and slightly deflects the drill bit to change the drilling direction. This method is known as horizontal or directional drilling. The horizontal drilling mechanism has a rigid connection to a thrusting system above ground, its diameter can be up to 500 mm and can drill up to several kilometers deep. In [10], a small radius of curvature for such systems was noted, its parameters are 114 mm diameter drill hole and 6,000 mm steering radius of curvature. Although these mechanisms can thrust using large forces, they do not fit through narrow gaps, they are limited in the path they can follow, are complicated and consume a great deal of energy to operate.

In our current work, we introduce a vibro-impact mechanism. By using two masses: main body and an actuator connected to a spring (as shown in Fig. 1), the robot can penetrate and propel itself underground. A similar mechanism was introduced in [11], and an extensive non-linear dynamics analysis was conducted, though this mechanism wasn't used for underground locomotion.

Robot locomotion underground may be affected by a variety of factors, such as different materials, moisture or density. In order to narrow down the problem to the scope of this research, we focus on autonomous robot locomotion in dry, granular, homogenous material, such as sand.

To achieve the ability to steer inside the granular medium we borrow an idea from medical robotics, using an asymmetric bevel-tip that causes the robot to move along a curved trajectory, e.g., [12]–[15]. Utilizing this asymmetry at the tip of a flexible needle, the operator can steer the needle in three-dimensions. By rotating the needle, hence changing the direction of the bevel, the needle can perform intricate 3-D motions [14]. Alterovitz et al. performed 2D path planning for the flexible bevel tip needle [12]. Given initial data on the needle location and orientation, bevel rotation and insertion distance, the suggested model would anticipate the next location allowing path planning and obstacle avoidance. A
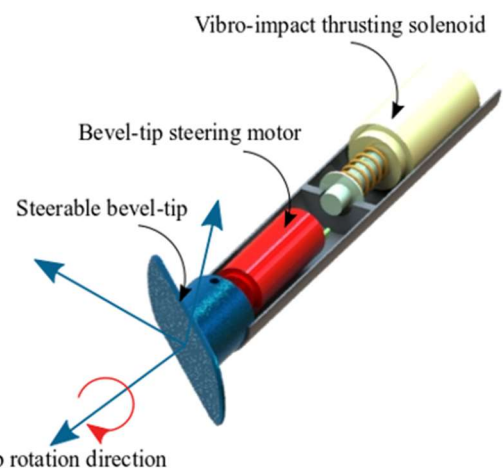
M. Barenboim is with the Technion Autonomous Systems Program, Technion – Israel Institute of Technology, Haifa 3200003 ISRAEL

A. Degani is with the Faculty of Civil and Environmental Engineering and with the Technion Autonomous Systems Program, Technion – Israel Institute of Technology, Haifa 3200003 ISRAEL (Email: adegani@technion.ac.il).

Figure 1 - Underground Steerable Robot CAD model and its cross-section

more recent work used nonholonomic motion planning, typically used for car models, to plan the steering of flexible needles [14]. This work suggests that by using nonholonomic modeling, control and path planning, a bevel-tip needle can reach a target location in a 3D environment. Unlike previous work, our proposed mechanism uses the bevel-tip steering concept inside a soil-like granular medium rather than in a tissue-like homogeneous ballistic gel. The concept of our underground robot is a stiff and short mechanism, fully submerged inside granular medium surface as opposed to the long and flexible needle used in the medical applications that extends above the surface.

In Sec. II, we briefly describe the mechanical design of our robot. In Sec. III, we present a model of the robot's trajectory using nonholonomic constraints, followed by a dynamic model of the internal thrusting mechanism. Using that model, we show the results of the numerical simulation. In Sec. IV we show validation of the model with experimental results on our robot and show that the experimental results agree with the predictions made in the simulation section. We conclude with discussion and future work in Sec. V.

II. MECHANISM DESIGN

The robot comprises a thrusting mechanism and a steering mechanism. The thrusting mechanism consists of a linear thrusting actuator connected through a spring to the robot's frame. Interaction of the bodies inertial forces, spring forces and non-conserving drag forces result in a net displacement over time when actuating the inner body. This type of thrusting mechanism exhibits motion without any externally moving parts. This may be significant in granular medium since the grains may interfere with exposed moving parts. The steering mechanism, placed in front, uses a DC-motor, which can rotate the bevel tip of the robot. With the rotation of the bevel tip, the robot's direction of motion can be controlled. The steering mechanism's design allows a three-dimensional trajectory, but in the scope of this work, we focus only on two-dimensional locomotion.

III. MODEL AND SIMULATION

In this section, we develop a model that describes the in-plane behavior of our robot. We separate the model into two parts. The first part describes the nonholonomic model for the steering mechanism and the second part describes the thrusting mechanism's dynamics. The two models can be decoupled based on the assumption that the motion underground is quasistatic and the high drag forces cause the robot to come to a stop at the end of each actuation cycle of the thrusting mechanism. Therefore, the dynamic effects of the thrusting on the steering model can be neglected. We introduce the simulation framework and the simulation results of the model.

A. In-plane steering kinematics

Exploiting the vast knowledge accumulated in needle steering for medical purposes, we model the bevel tip mechanism as a simple kinematic car, widely known as the bicycle model [16]. In this model, the rear end of the robot is constrained to have a zero sideways velocity. In the front end of the robot, where the bevel tip is located, there is a second velocity constraint, perpendicular to the steering direction, marked ϕ_0, as depicted in Fig. 2. The steering direction and
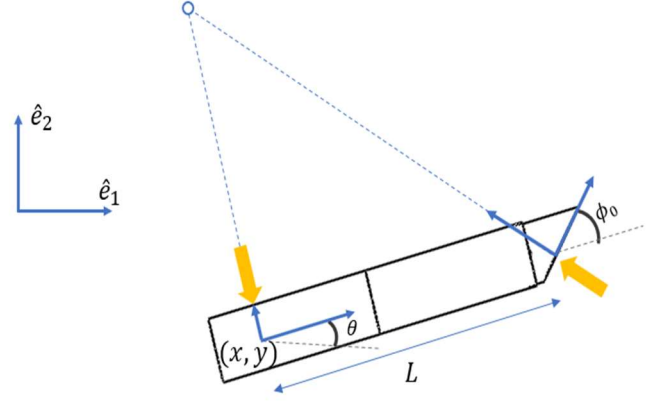

Figure 2 - Schematic description of the bevel-tip robot, constraints direction and center of rotation.

the bevel-tip direction are not necessarily equal. The steering direction is the kinematic model parameter and is being found in the experiments section, while the bevel-tip direction is a design parameter of the physical robot.

Keeping notation similar to [16], the robot's position and orientation are defined on a 2D plane. We denote the position of the rear end of the robot in a Cartesian plane with (x, y) and its orientation θ defined as the angle between the robot's cylinder axis and the global x-axis $(\hat{e}_1)$. The configuration, describing the robot's pose, is defined as $q_1 = (x, y, \theta)^T$. We define ϕ_0 as the steering angle of the robot. The Pfaffian constraints on the robot are

$$sin(\theta + \phi)\dot{x} - cos(\theta + \phi)\dot{y} - Lcos(\phi)\dot{\theta} = 0 \qquad (1)$$

$$sin(\theta)\dot{x} - cos(\theta)\dot{y} = 0 \qquad (2)$$

The equations for the kinematic model of the robot are

$$\dot{x} = cos(\theta) \cdot u_1$$
$$\dot{y} = sin(\theta) \cdot u_1$$
$$\dot{\theta} = \frac{1}{L}tan(\phi) \cdot u_1 \qquad (3)$$

Constraints (1) and (2) are satisfied by (3). The robot's length is denoted L and u_1 is a scaling factor, since any scalar multiple of the solution will satisfy (1) and (2). As mentioned earlier, we focus on motion in a two-dimensional plane. For this purpose, we further restrict the model to only allow binary steering direction change, $\phi = \pm\phi_0$, similar to Dubins car [17], but without the ability to move straight. A simple simulated trajectory is shown in Fig. 3.

B. Modeling the thrusting mechanism

As discussed in the introduction, the forward motion of the robot is achieved by using a vibro-impact mechanism. A relatively simple vibro-impact mechanism includes two bodies connected by a spring. This type of mechanism exhibits stick-slip transitions under Coulomb's friction model. Both bodies are allowed to stick or slip relative to each other and relative to a fixed coordinate frame, making the system a multi-body, hybrid, dynamical system [18]. The robot is designed so that the first body, denoted m_1, is the outer shell of the robot including the steering mechanism's mass. The second body,
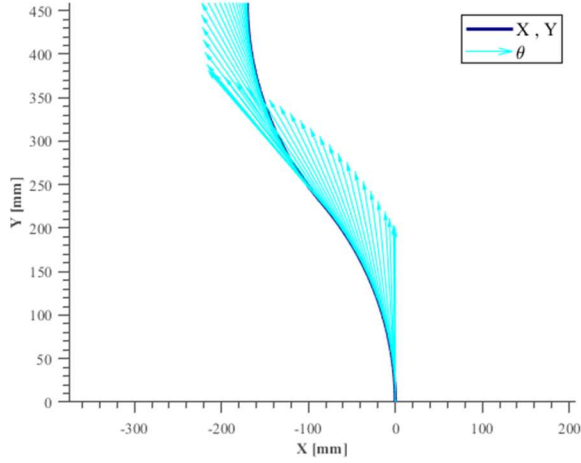
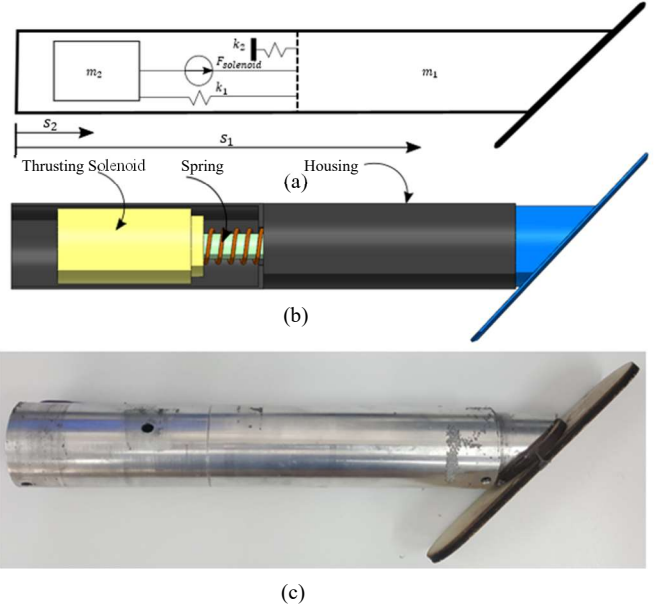Figure 3 - Simulated trajectory using bicycle kinematic model.

Figure 4 - (a) Model of the thrusting mechanism including linear actuator, spring and an impact spring. (b) Schematic model describing the main parts of the thrusting mechanism. (c) Photograph of the proof-of-concept mechanism.

m_2, is the inner mass serving as the thrusting actuator. A description of the thrusting mechanism is shown in Fig. 4.

We formulate the equations of motion using a set of generalized coordinates, $q_2 = [s_1, s_2]^T$, where s_1 and s_2 represent the outer and inner body's translation along the robot's trajectory respectively (depicted in Fig. 4).

The vibro-impact mechanism design allows the spring to reach its solid length. When this event occurs, it limits the internal body translation relative to the external body and applies higher forces on both. To model this effect, we add a hybrid high stiffness spring, k_2, which is toggled on and off in the simulation according to the bodies' relative positions. The hybrid spring condition is $s_2 - s_1 < 0$, denoted $J(s_2 - s_1)$, a Heaviside step function [19]. Following this, the dynamic equations, using Lagrangian mechanics, are given as

$$M\ddot{q} + G(q) = \bar{F}_{solenoid} + W \cdot \Lambda$$

where,

$$M = \begin{pmatrix} m_1 & 0 \\ 0 & m_2 \end{pmatrix},$$

$$G(q) = \begin{pmatrix} k_1(s_1 - s_2) + J \cdot k_2(s_1 - s_2) \\ -k_1(s_1 - s_2) - J \cdot (s_1 - s_2) \end{pmatrix},$$

$$\bar{F}_{solenoid} = \begin{pmatrix} F_{solenoid} \\ -F_{solenoid} \end{pmatrix},$$

(4)

$$W = \begin{pmatrix} 1 & 0 \\ 0 & 1 \end{pmatrix},$$

$$\Lambda = \begin{pmatrix} \lambda_1 \\ \lambda_2 \end{pmatrix}.$$

The generalized actuating force between the two bodies is denoted as $F_{solenoid}$ and will be further discussed in the simulation section (Sec. III D). The constraint forces, denoted $\Lambda = [\lambda_1, \lambda_2]^T$, are obtained by Lagrange's multipliers, representing the friction forces. In order to allow a slip transition, the condition $|\lambda_i| > f_i$, $(i = 1,2)$ must be satisfied. The drag forces, f_1, between the granular medium and the robot and f_2 is the Coulomb friction force which should satisfy $|\lambda_2| \geq \mu_2 N_2$.

When the outer body remains in place relative to the global coordinate frame, or the inner body remains in place relative to the outer body, their states are denoted as a Stick state. Table I summarizes the states and the conditions that are needed to be met in order to change a current state to a new state. When the outer or the inner bodies move relative to the global coordinate frame or relative to each other, their state is denoted

TABLE I. STATE TRANSITION TABLE

Old State	New State			
	Stick-Stick	Slip-Stick	Stick-Slip	Slip-Slip
Stick-Stick	-	$\|\lambda_1\| - f_1 > 0$	$\|\lambda_2\| - \mu_2 m_2 g > 0$	$\|\lambda_1\| - f_1 > 0$ && $\|\lambda_2\| - \mu_2 m_2 g > 0$
Slip-Stick	$\dot{s}_1 = 0$ && $\|\lambda_1\| - f_1 < 0$	-	-	$\|\lambda_2\| - \mu_2 m_2 g > 0$
Stick-Slip	$\dot{s}_2 = 0$ && $\|\lambda_2\| - \mu_2 m_2 g < 0$	-	-	$\|\lambda_1\| - f_1 + sgn(\dot{s}_2)\mu_2 m_2 g > 0$
Slip-Slip	-	$\dot{s}_1 = 0$ && $\|\lambda_1\| - f_1 < 0$	$\dot{s}_2 - \dot{s}_1 = 0$ && $\|\lambda_2\| - \mu_2 m_2 g < 0$	-

as *Slip state*. The possible states of the thrusting mechanism are denoted as *Stick-Stick, Slip-Stick, Stick-Slip* and *Slip-Slip*. The first term refers to the state of the outer body, the latter refers to the inner body. It is assumed that two transitions cannot be made at the same instant, therefore some of the transitions are not allowed.

C. Drag forces in granular medium

To model the reaction forces acting on the robot, we approximate the small grains of the granular material as a continuous medium applying pressure on the robot, consequently creating a normal force. Similar to Coulomb's friction law, we assume that tangential forces are proportional to the normal force, $f_2 = \mu_2 \cdot F_n$, where μ_2 is the coefficient of friction and F_n is the normal force. Analogous to a notion presented in [20], we assume that the pressure inside the granular medium increases linearly with depth, and can be written in the form of $\sigma(d) = \gamma \rho g |d|$, where $|d|$ is the depth measured from the upper surface of the granular medium, ρ is the granular medium density, g is gravitational acceleration, and γ is a constant drag coefficient that will be tuned empirically. The normal force can then be found by integrating the pressure acting on the surface of the robot

$$\bar{F}_n = \iint \sigma(d) \cdot \bar{n} \cdot dA, \tag{5}$$

where, $\bar{n}$ is the normal to the surface of the robot, and A is the surface area parametrization.

D. Dimensionless analysis of thrusting mechanism model

Two assumptions are made to simplify the mechanism's equations of motion; First, the inner and outer bodies are assumed to be point masses, which is a feasible assumption since the inertial terms were modeled with respect to the bodies' mass and not their dimensions. Second, since the inner mass slides on a bearing with low friction, the friction f_2 can be neglected relative to the drag forces of the whole body. The characteristic time and length scales for this non-unique set are chosen to be $\sqrt{m_1/k_1}$ and $F_{solenoid}/k_1$, respectively. The terms $(1/2\pi)\sqrt{m_1/k_1}$ and $F_{solenoid}/k_1$ correspond to the resonant frequency and the distance the mass moves per unit force of a simple harmonic oscillator. The dimensionless analysis results in a more compact form of the equations of motion

$$\frac{d^2\chi_1}{d\tau^2} + (1 + J\kappa) \cdot (\chi_1 - \chi_2) =$$
$$F(\tau) - \text{SlipSign}\left(\frac{d\chi_1}{d\tau}\right) \cdot \alpha \tag{6}$$
$$\frac{d^2\chi_2}{d\tau^2} + (1 + J\kappa) \cdot (\chi_2 - \chi_1) = -F(\Omega \cdot \tau)$$

where, $\chi_i = s_i \cdot k_1/F_{solenoid}$ and $\tau = t \cdot \sqrt{k_1/m_1}$ are the non-dimensional position coordinates and time. SlipSign denotes the velocity direction relative to the global coordinate frame. Nondimensionalizing the equations of motion reduces the number of parameters from four to two, $\alpha = f_1/F_{solenoid}$ and $\kappa = k_1/k_2$. The values of the parameters used in the dimensionless analysis and in the rest of this work are presented in Table II.

TABLE II. PARAMETERS FOR MODELING SIMULATION

Parameter	Description	Value
m_1	Inner body mass	0.164 kg
m_2	Outer body mass	0.3 kg
L	Length between no-slip constraints	0.2 m
ϕ_0	Steering angle	22 °
μ_1	Friction coefficient between inner and outer bodies	0.05
μ_2	Equivalent friction coefficient between the outer body and the granular medium (Aluminum and glass bead)	0.2[a]
g	Gravitational acceleration	9.81 m/s²
ρ	Granular medium density	1510 kg/m³
k_1	Spring coefficient	244 N/m
k_2	Hybrid spring coefficient	2500 N/m
γ	Drag coefficient	0.5
α	Solenoid coefficient	200 N/m

a. Aluminum-Glass bead coefficient approximated from [22]

E. Numerical Simulation Results

The aim of this section is to provide a control design tool and to allow further exploration of the dynamics with different control parameters. The simulations were conducted using MATLAB™ ode solver, while the hybrid instances (i.e., slip-stick transitions) were detected using the event function.

The force that the actuator applies is subject to the system's state. The electric solenoid is based on a magnetic field that weakens as the plunger exits the coil. Thus, the solenoid can generate its maximum force only when the plunger is fully inserted into the solenoid coil [21], i.e., when the two bodies are at a minimum distance. The actuator's force is approximated by the linear, first-order equation

$$F_{solenoid}(s_1, s_2) = \eta \cdot (F_{Solenoid\,Max} - \alpha_{Solenoid} \cdot (s_1 - s_2)), \tag{7}$$

where η is a simple square-wave signal that activates and deactivates the solenoid force function and α is the solenoid coefficient.

Fig. 5 displays the non-dimensional translation of the outer and inner bodies, χ_1, χ_2 respectively. The control signal parameters are $f_\eta = 10$ Hz and $F_{Solenoid\,Max} = 2$ N for the square wave frequency and the solenoid's amplitude. As seen in the figure, although the bodies displacement exhibits an oscillatory motion, net motion is achieved.

Next, we simulate a control input "parameter sweep", with the aim of mapping the influence of different control parameters on the locomotion performance. In the thrusting part of the simulation, the control input parameters are the frequency and magnitude of the force between the inner and outer bodies. Surprisingly, both the change of frequency and
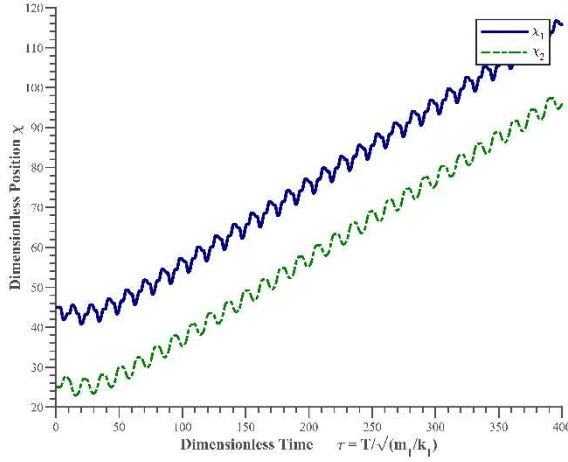
Figure 5 - Simulated thrusting mechanism translation of outer body χ_1 and inner body χ_2.

amplitude will not only cause a change of moving speed but, with careful choice of either one, the direction of movement can be reversed. A contour map showing the average velocity obtained by different combinations of input-signal parameters is presented in Fig. 6. In the figure, a black circle describes the parameters chosen for forward movement presented above in Fig. 5. Fig. 7 shows the simulation results of reversed motion, achieved by choosing parameters in the reversed area in the contour map, marked by a red circle in Fig. 6.

IV. EXPERIMENTS AND MODEL VALIDATION

We conducted experiments to tune and validate the proposed model. First, we present the experimental setup and discuss the robot design based on simulations and some of the experiment limitations. Then, we conclude with a proof-of-concept experiment showing the feasibility of path planning. See supplementary material for a video of these experiments.

A. Experimental setup and robot design

The experimental setup comprises a small container sized 0.5 x 0.3 x 0.8 m³. We used 1-1.5 mm diameter sphere-shaped glass beads as a homogeneous granular medium. A Vicon
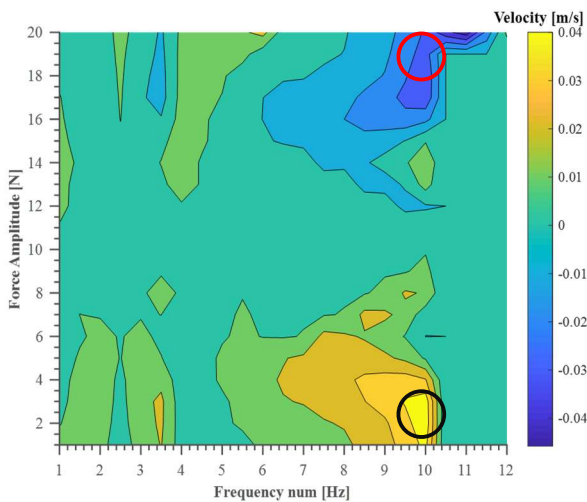

Figure 7 - Contour map describing the direction of motion and velocity given a different input signal to the robot. Black and red circles show the values used in the numerical simulations of Figure 5 and Figure 6, respectively.

T10S motion tracking system was used to record the robot's trajectory and measure its radius of curvature. To identify the robot's pose in space, we placed reflective markers on the robot that allow a 2 mm measurement accuracy. Since the robot is mostly underground, we connected the markers to beams protruding outside and visible to the cameras. We conducted an additional experiment to show the change in direction of the robot, on which we accurately measured the robot's displacement using BAUMER ODAM12 laser sensor, with resolution of 2-5 μm and National Instruments signal acquiring system, at 1,000 Hz.

Throughout the experiments, we discovered that the steering angle of the robot is affected not only by the bevel-tip but also by the length of the robot. This is logical since a longer robot may present a longer distance between the equivalent reaction forces that oppose the moment (shown above in Fig. 2) causing the robot to turn in the yaw direction. It is also expected with the kinematic bicycle model, as the radius of curvature is affected by the length and the steering angle, as in (2). To allow rotation of the bevel tip, we had to elongate the robot to add a DC-motor. This elongation increased the turning radius significantly. To cope with the elongation, we increase the contact surface area of the bevel tip, as shown in Fig. 8. By doing so, we decreased the radius of curvature, with the downside of increasing the drag on the robot causing it to move slower. The optimization of the bevel-tip length relative to its body length is set aside for future research.

B. Model validation and results

To fit the parameters, we tested the trajectory output in three different depths: 30 mm, 45 mm, and 65 mm, measured from the surface level to the cylinder's axis. The trajectory obtained were fitted to a circle, with radius parameter fit of $P_{30} = 327$ mm, $P_{45} = 252$ mm, $P_{65} = 254$ mm, as shown in Fig. 9. The different values of radius of curvature obtained can be explained in the following way: it is obvious that actuating the robot on land will not cause its yaw angle to change since some reaction force perpendicular to the steering angle is needed. Keeping this in mind, actuating in shallow depth will cause the robot to turn with a larger radius of curvature. As the robot deepens, the reaction effect of the granular medium is more significant, since more pressure is applied to the robot. We therefore assume a boundary layer in the shallow depths. In trajectories that were measured deeper than 45 mm, the
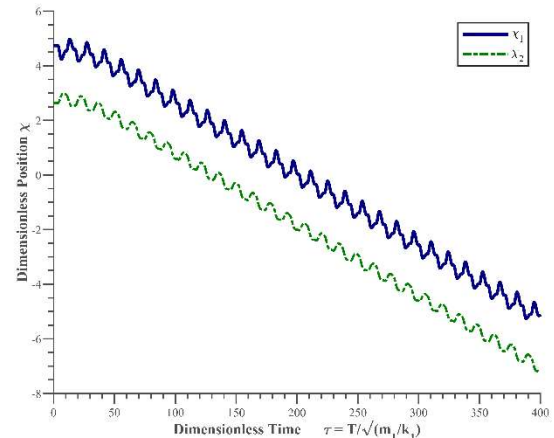

Figure 6 - Simulation result shows steady reversal motion of the robot with a carful choice of force amplitude while keeping the same frequency.

833

Figure 9 - Reflective markers connected above the robot so that trajectory can be measured while the robot is underground.

radius of curvature remained constant. After measuring the radius of curvature, the steering angle was calculated using (2).

As discussed in Sec. II, with careful choice of the input parameters, amplitude and frequency, motion direction can be reversed. We validated the numerical simulation results of the thrusting mechanism. Fig. 10 shows three displacement measurements along time, for three different voltage levels used for excitation. A fixed input frequency of $f = 5.56$ Hz was used in all three experiments. Fig. 10 (a) shows a reversed displacement with $V_{in} = 8.5$ V. In Fig. 10 (b) the amplitude used is $V_{in} = 10$ V, and exhibits a reciprocal motion with no net displacement along time. Fig. 10 (c) shows forward motion given $V_{in} = 11.5$ V.

We conclude with a proof-of-concept experiment. Using the model parameters found above, we show the trajectory of the robot in a 2D plane in Fig. 11. We performed the experiment using an open-loop control, with a constant input voltage $V_{in} = 11.5$ V, constant frequency $f = 5$ Hz and changing the steering angle once $\phi_{0_i} = 0°$, $\phi_{0_f} = 180°$. By changing the steering angle ϕ at a chosen pose it is feasible to perform a motion planning algorithm, as suggested in [12].

V. CONCLUSION

Several studies were done with the aim of designing a robot that can pave its own path underground. However, most of the work done thus far focused either on robots that are rigidly connected above surface and can perform limited trajectories, or untethered robots that can solely move straight. There has been little research reported on non-rigidly attached robots that are also able to maneuver underground. The purpose of this study is to design a robot that can do both. In this paper, a simple mechanical design is presented, that achieves net motion with an internal mechanism propelling itself and a bevel-tip head that steers toward the desired direction. A simplified dynamic model of the thrusting mechanism and kinematic model of the bicycle model was introduced and was used to perform numerical simulations. Using the simulations, a parameter sweep was conducted showing a connection between the parameters of the input signal and the robot's direction of motion. By carefully choosing the input parameters, frequency and force amplitude, the robot was able to move in reversed direction. Several proof-of-concept experiments showed the feasibility of moving within granular medium in different depths, including a change of steering direction.

With the end-goal of a fully maneuverable underground robot, future work will focus on three-dimensional analysis. Such a model will help develop motion planning algorithm that will consider the dependence between radius of curvature
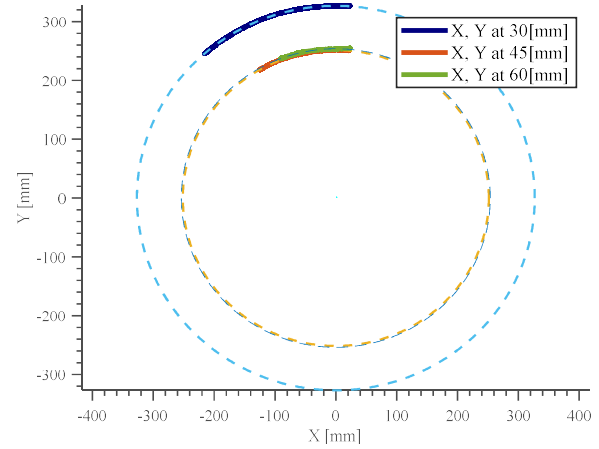

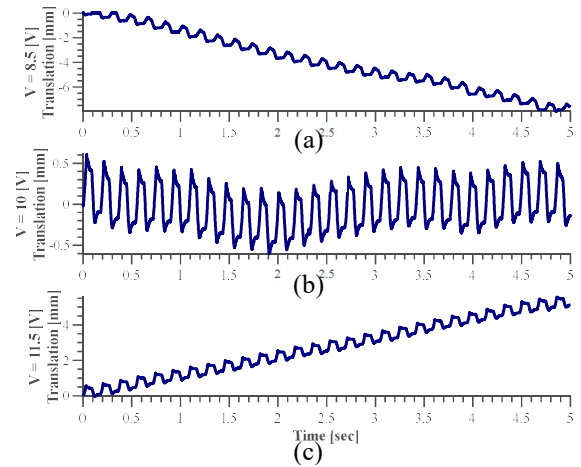Figure 8 - Radius of curvature measured in experiments at three different depths.

Figure 10 - Translation measured at constant input frequency f=5.56 Hz, and different input voltage.
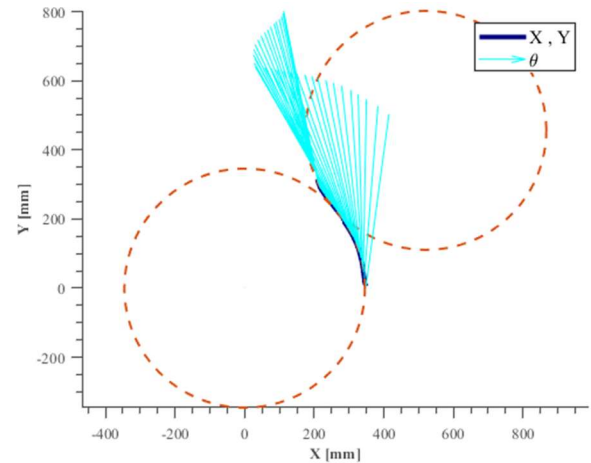

Figure 11 – Trajectory measured in an experiment, including rotation of the bevel tip midway, to change direction.

and the robot's depth. Further design will also include on-board sensing, replacing the Vicon camera system with internal sensors, such as accelerometers, to approximate the robot's position and orientation. Additionally, the presented study is limited to homogenous glass-bead medium; further work will target additional granular mediums.

REFERENCES

[1] F. Becker, S. Börner, R. Lichtenheldt, and K. Zimmermann, "Enabling Autonomous Locomotion into Sand – A Mobile and Modular Drilling Robot State of the art," in *Proceedings of ISR: 47st International Symposium on Robotics*, 2016, pp. 307–312.

[2] T. Dewei, Z. Weiwei, J. Shengyuan, S. Yi, and C. Huazhi, "Development of an Inchworm Boring Robot(IBR) for planetary subsurface exploration," in *IEEE International Conference on Robotics and Biomimetics, IEEE-ROBIO*, 2015, pp. 2109–2114.

[3] A. Greene, "Biologically Inspired Mechanisms for Burrowing in Undersea Substrates," Ph.D. dissertation, Dept. Mech. Eng. Massachusetts Institute of Technology, 2011.

[4] A. Koller-hodac *et al.*, "Actuated Bivalve Robot Study of the Burrowing Locomotion in Sediment," in *IEEE International Conference on Robotics and Automation*, 2010, pp. 1209–1214.

[5] R. A. Russell, "CRABOT: A biomimetic burrowing robot designed for underground chemical source location," *Adv. Robot.*, vol. 25, no. 1–2, pp. 119–134, 2011.

[6] K. Zacny, D. Boucher, P. Coste, B. Derkowski, R. Fincher, and B. Glass, *Chapter 6 : Extraterrestrial Drilling and Excavation*. 2009.

[7] L. Richter and O. Kroemer, "Application of a Remote Controlled Hammering Drill from Space to Deep Sea," in *OCEANS*, 2009, pp. 1–4.

[8] R. Lichtenheldt, B. Schäfer, and O. Krömer, "Hammering beneath the surface of Mars – Modeling and simulation of the impact-driven locomotion of the HP3-Mole by coupling enhanced multi-body dynamics and discrete element method," in *58th Ilmenau Scientific Colloquium IWK*, 2015.

[9] R. Lichtenheldt, F. Becker, and K. Zimmermann, "Screw-driven Robot for Locomotion into Sand," in *59th ILMENAU SCIENTIFIC COLLOQUIUM*, 2017, pp. 11–15.

[10] National Research Council, *Drilling and Excavation Technologies for the Future*. Washington, DC: The National Academies Press, 1994.

[11] Y. Liu, E. Pavlovskaia, M. Wiercigroch, and Z. Peng, "Forward and backward motion control of a vibro-impact capsule system," *Int. J. Non. Linear. Mech.*, vol. 70, pp. 30–46, 2015.

[12] R. Alterovitz, K. Goldberg, and A. Okamura, "Planning for steerable bevel-tip needle insertion through 2D soft tissue with obstacles," in *IEEE International Conference on Robotics and Automation*, 2005, pp. 1640–1645.

[13] V. Duindam, R. Alterovitz, S. Sastry, and K. Goldberg, "Screw-based motion planning for bevel-tip flexible needles in 3D environments with obstacles," in *IEEE International Conference on Robotics and Automation*, 2008, pp. 2483–2488.

[14] R. J. Webster, N. J. Cowan, G. Chirikjian, and A. M. Okamura, "Nonholonomic modeling of needle steering," *Springer Tracts Adv. Robot.*, vol. 21, pp. 35–44, 2006.

[15] S. Misra, K. B. Reed, B. W. Schafer, K. T. Ramesh, and A. M. Okamura, "Mechanics of flexible needles robotically steered through soft tissue," *Int. J. Rob. Res.*, vol. 29, no. 13, pp. 1640–1660, 2010.

[16] R. M. Murray, Z. Li, and S. S. Sastry, *A Mathematical Introduction to Robotic Manipulation*, vol. 29. CRC Press, 1994.

[17] L. E. Dubins, "On Curves of Minimal Length with a Constraint on Average Curvature, and with Prescribed Initial and Terminal Positions and Tangents," *Am. J. Math.*, vol. 79, no. 3, pp. 497–516, 1957.

[18] H. Schumacher, *An Introduction to Hybrid Dynamical Systems*. pp. 49-50, 1999.

[19] R. Bracewell, *The Fourier Transform And Its Applications*, 3rd ed. New York: McGraw-Hill, pp. 61, 2000.

[20] T. Zhang and D. I. Goldman, "The effectiveness of resistive force theory in granular locomotion," *Phys. Fluids*, vol. 26, no. 10, 2014.

[21] P. H. Schimpf, "A Detailed Explanation of Solenoid Force," 2013.

[22] B. Suhr and K. Six, "On the effect of stress dependent interparticle friction in direct shear tests," *Powder Technol.*, vol. 294, 2016.

835